Tough Composites Inspired by Mineralized Natural Materials: Computation, 3D printing, and Testing

*Leon S. Dimas, Graham H. Bratzel, Ido Eylon, and Markus J. Buehler**

Composites play an important role as structural materials in a range of engineering fields due to their potential to combine the best mechanical properties of their constituents. In biology, composites are ubiquitous and exhibit fascinating and precise architectures at fine length scales; bone, hexactinellid sponges and nacreous abalone shells are prime examples. Here, typical biological composite topologies are emulated with multi-material 3D printing at micrometer resolution. From base materials that are brittle and exhibit catastrophic failure, synthetic composites are created with superior fracture mechanical properties exhibiting deformation and fracture mechanisms reminiscent of mineralized biological composites. This complementary computational model predictions of fracture mechanisms and trends in mechanical properties are in good agreement with the experimental findings. The reported findings confirm that specific topological arrangements of soft and stiff phases as a design mechanism enhances the mechanical behavior in composites. This study demonstrates 3D printing as a means to create fracture resistant composites. Moreover, these results indicate that one can use computer models to design composite materials to exhibit tailored fracture properties and then use 3D printing to synthesize materials with such mechanical performance.

1. Introduction

In nature, and particularly among the class of mineralized materials, it is common to find composites that combine simple constituents with primitive mechanical characteristics in complex architectures to form composite structures with fracture mechanical properties far exceeding that of their building blocks. Understandably, these materials have attracted a great deal of interest and are well studied by the materials science research community.[1–12] Computational modeling and theoretical analysis have also been essential tools in the effort of elucidating the design principles of these complex structures.[13–17]

In addition to research efforts devoted to further understanding the fundaments of strength of these mineralized composites, there is an obvious interest in developing methods with the potential of synthesizing composites with equally impressive mechanical characteristics. Techniques such as self-assembly and layer-by-layer (LBL) templating have been popular in this regard. The accomplishments to date are nothing short of remarkable.[18–23] While both techniques are very powerful and have the potential for a precise control of structural features at very fine length-scales, to the best of the authors' knowledge, to date neither of the methods provides an outlook for large-scale cost-effective manufacturing of complex topologies, in particular at larger hierarchical length-scales.

Three-dimensional (3D) printing has as of late been gaining much attention due to its many possible applications in a wide range of industries; indeed exploring the areas of applicability of the technique is still an active area of research.[24–31] With the latest 3D printers capable of printing materials with widely contrasting mechanical behavior simultaneously in complex geometries at micrometer resolutions, the potential of this technology is growing. Advanced printing technology now offers the possibility to create complex topologies with fine features composed of a multitude of materials with varying mechanical properties quickly, cheaply and at a large scale.

In our previous work we have developed meso-scale molecular mechanics models and have simulated bio-inspired composites that exhibit fracture mechanical properties far superior to their constituents.[17,32,33] Here we employ state of the art 3D printing as a simple and effective rapid manufacturing technique and create physical artifacts of these computational systems, by printing composites with bio-inspired topologies that exhibit structural properties similar to our computational models and far superior to their constituents. A process flow of our work is presented in **Figure 1**. The specific geometries we printed are a bone-like geometry, bio-calcite-like geometry

L. S. Dimas, G. H. Bratzel, Prof. M. J. Buehler
Laboratory for Atomistic and Molecular Mechanics
Department of Civil and Environmental Engineering
Massachusetts Institute of Technology
77 Mass. Ave. Room 1-235A&B, Cambridge,
MA 02139, USA
E-mail: mbuehler@mit.edu
G. H. Bratzel
Department of Mechanical Engineering
Massachusetts Institute of Technology
77 Mass. Ave. Cambridge, MA 02139, USA
I. Eylon
Stratasys Ltd.
5 Fortune Drive, Billerica, MA 01821, USA

DOI: 10.1002/adfm.201300215

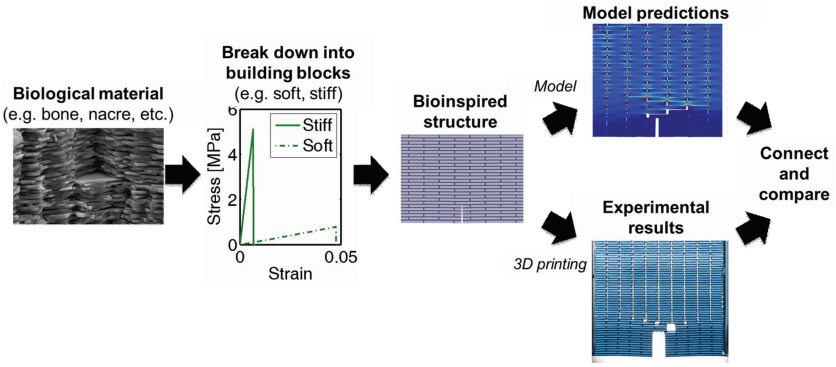

Figure 1. Process flow of the approach used here. Starting from the simple model material building blocks, we build composites with bio-inspired topologies. We manufacture the bio-inspired composites with 3D printing and proceed to test the synthesized specimens. The results are compared to model predictions.

and a rotated bone-like geometry consisting of a stiff and a compliant phase with a ≈20% volume fraction of the softer phase (**Figure 2**).[32] The optimal volume fraction is bound from below by the desire to keep the computational system small and tractable, and bound from above by the objective to maintain structural rigidity of the composite. A volume fraction of 20% was found to balance these two requirements in a satisfactory manner. We further investigate the specific deformation and fracture mechanisms induced by the various topological arrangements in the experimental systems and obtain encouraging results. Our results indicate the possibility of designing materials with computers with tailored fracture mechanical properties and later realizing these structures with 3D printing.

2. Results

We first investigate the fracture response of the two base materials used for printing the composite geometries, material **A** and material **B**. Results are shown in **Figure 3**, and further details are provided in the Experimental Section. Having investigated the fracture response of the two base materials, we proceed to studying the deformation and fracture mechanisms of the bio-inspired hierarchical geometries shown in Figure 2a. We begin with studying the mechanical response of the 3D printed bone-like topology consisting of stiff platelets ordered in a compliant matrix.

2.1. Comparison of Computational Predictions with Experiment

In **Figure 4** we present a representative set of images comparing the deformation and fracture mechanisms of the 3D printed sample (Figure 4a) with the corresponding mechanisms of the simulated specimen (Figure 4b). The printed specimens are all 3.125 mm thick in the out of plane direction. As predicted by our computational model, this specific topological arrangement induces significant stress and strain delocalization, which we confirm in the 3D printed system. This is clearly visualized through the non-localized failure of the vertical compliant phase throughout the entire specimen. The continuous compliant matrix phase distributes stress and strain effectively throughout the sample, inducing a more robust mechanical response of the geometry. For the simulation results depicted in Figure 4b, the delocalization is visualized in terms of snapshots of the longitudinal strain fields of the specimen. The vertical portion of the compliant phase adsorbs the bulk portion of longitudinal strain whilst the horizontal portion of the softer matrix binds the system together through shear strain action. This deformation mechanism exhibited by our computational and synthetic system is characteristic of mineralized natural materials such as bone.[14] For both our computational prediction and the experimental system, this deformation mechanism is activated by minor initial crack propagation. In the inset of Figure 4a we highlight another remarkable trait of the 3D printed specimens. As noted in the Experimental Section, the interfacial adhesion of the constituent materials is so strong that the composites do *not* fail at the interfaces. This is compatible with our computational prediction and underlines the significance of the topological arrangements for the mechanical behavior. Indeed, we argue that the particular topological arrangements of the constituent materials are solely responsible for the impressive observed fracture mechanical characteristics. The strong interfaces form upon printing and are not induced by any special treatment of the materials.

Upon further crack propagation our prediction diverges from the experimentally observed behavior. As noted in the Experimental Section, crack propagation induces eccentricity in the experimental loading conditions, whilst the computational boundary conditions remain

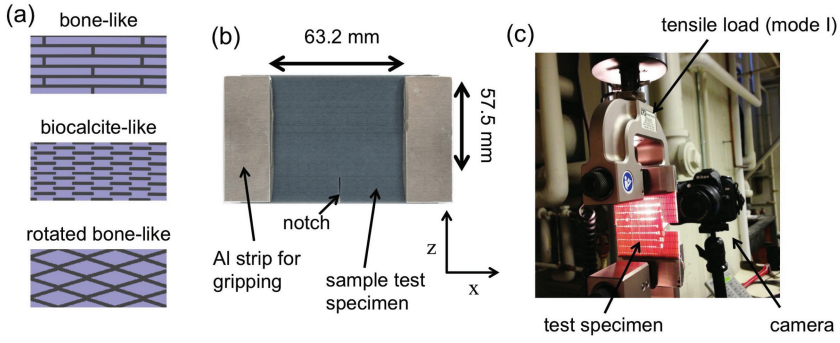

Figure 2. a) Schematics of the three investigated topologies. b) Setup of test specimens with relevant dimensions and coordinate system indicated. c) Image of the setup of the experiment. A specimen of the bone-like geometry is being tested in the picture, shown here as an example.

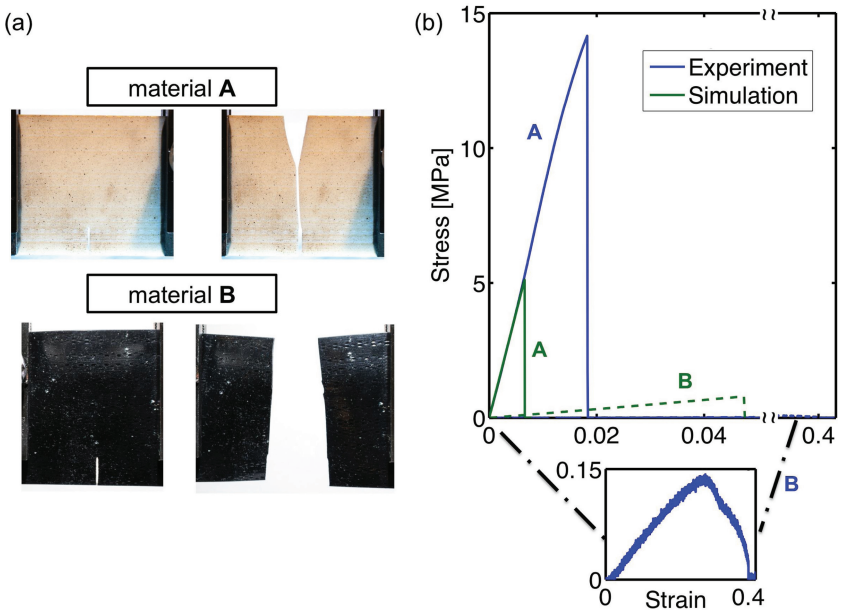

Figure 3. Images of samples at the start of testing, the end of testing and graphs of stress-strain response for base materials, material **A** and material **B**, as well as their computational equivalents. a) Images of test specimens of material **A** and material **B** before and after testing. Pictures indicate brittle catastrophic failure of the base materials. b) Stress versus strain behavior of experimental and computational base materials drawn in blue and green respectively. The modulus of computational equivalent of material **A** is seen to match with its experimental counterpart. Further, the extreme compliance of material **B** makes it barely visible on the original plot and thus its notched stress strain response is included in an inset of the figure. The computational equivalents of material **A** and **B** are designed to fail at lower strains to avoid geometrical instabilities in the model. Further, the computational equivalent of material **B** is designed with a more humble compliance to avoid instabilities in the simulation and to also more closely resemble the average mechanical properties of the printed compliant phase (see discussion in the Experimental Section).

constant throughout the simulation. The crack tip region in the experimental setup is subjected to a different stress field and thus produces an incompatible effect on crack propagation. Although the cracked samples of the constituent materials behave linearly up to fracture, the constitutive response of the uncracked specimens is highly nonlinear, characteristic of polymers. As also discussed in the Experimental Section, these nonlinearities are expected to have a significant effect on crack-propagation.

Next we analyze the agreement between simulation and experiment regarding the fracture and deformation mechanisms exhibited by the 3D printed bio-calcite-like and rotated bone-like topology samples. **Figure 5** compares the computationally predicted results with the experimentally obtained behavior for these two composite systems. First, analyzing the rotated bone-like system in Figure 5a, the images clearly portray that the 3D printed sample exhibits impressive mechanical characteristics in terms of stable fracture propagation. Again we plot longitudinal strain fields along with snapshots from the simulation to identify the underlying mechanical mechanisms controlling the failure of the specimen. The characteristic initial zigzag fracture path through the compliant phase exhibited by both the experimental and the computational system is seen to be explainable by the continuous transfer of longitudinal strain in the soft matrix. As it is energetically favorable for cracks to propagate through a more compliant material, and the stiffness mismatch is so significant that the fracture propagates solely through the matrix. Further, as the crack-tip is blunted in the low-stiffness region and the soft matrix delocalizes the loading, the crack propagates in a stable fashion through the system allowing the specimen to sustain increased deformation and significant loading throughout large portions of the fracture process.

Analyzing the further images of Figure 5a, we note that the second row of images from experiment and simulation indicate a diverging fracture path. The boundary condition that acts eccentrically upon initial crack propagation induces the inclined driving force on the crack and leads the fracture towards the boundary.

In Figure 5b we compare and contrast simulation predictions and experimental observations for the response of the bio-calcite like topology. Although we observe that this topology has not been replicated well by 3D printing, the properties of the synthesized sample are still worth discussing. The inset in Figure 5b highlights the discrepancies between the 3D printed geometry and the computationally conceived topology. Whereas the soft inclusions are rectangles in the computational model, they resemble ellipses in the synthesized specimen. The surface area of the soft phase is notably larger for this topology, and we expect the inaccurate synthesized geometry to be caused by material mixing at the interface of the soft and stiff phase. In the Experimental Section we provide additional comments on the inaccuracies of printing for this geometrical configuration. The images clearly portray that the 3D printed sample possesses fracture mechanical characteristics superior to its constituents exhibiting both stable crack propagation and significant crack-tip blunting prior to main crack propagation. The latter toughening mechanism is highlighted in the inset of the figure, where we see that the initial fracture propagation leads the crack to soft inclusion where the extreme compliance blunts the crack tip and hinders crack propagation. Once the crack propagates, we again see that it angles out to the boundary due to the resulting eccentricity of the applied load.

Turning our attention back to the inaccuracies of printing for the bio-calcite-like topology, we do not expect significant agreement between simulation and experiment for this case (**Figure 6**), although the snapshots from simulation do provide some overlapping mechanisms. In future work there are

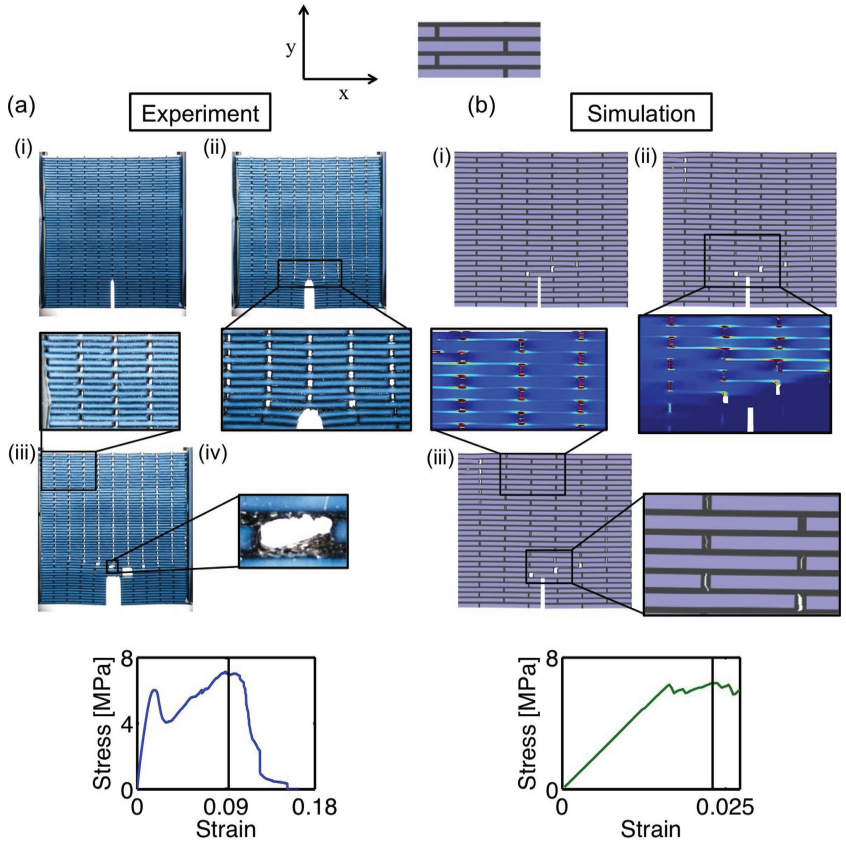

Figure 4. We present snapshots displaying deformation and fracture mechanisms for a) the 3D-printed and b) simulated specimen of the bone-like topology, in direct comparison. The two samples exhibit very similar deformation and fracture mechanisms up to a certain point at which the change of boundary conditions in the experiment and the nonlinearities of the photopolymers start dominating. This instant is indicated with a vertical line in the stress versus strain plots. The Figure shows that in both the synthetic and computational system the soft phase absorbs the bulk of the deformation and acts to delocalize the stress concentration around the notch. For the computational case shown in (b) we plot longitudinal (*x*-direction) strain fields in insets to make this clearer. Furthermore, the inset in (a) (iii) displays the strong interfacial adhesion of material **A** and material **B** with failure nucleating through the compliant material **B** instead of at the interface. This is consistent with the results of our computational model. The printed specimens are all 3.125 mm thick in the out of plane direction.

two phases in a two-phased composite was shown to play an essential role in the distribution of stresses and strains prior to initial crack propagation. Appropriate stiffness ratios can actually alleviate stress concentrations in flawed specimens thereby moderating the tendency of a composite to fail in a brittle manner.[34]

In Figure 6a–b we show a bar plot comparing select fracture mechanical characteristics of the various experimentally tested and simulated specimens respectively. We perform the comparison using data from experiment and simulation up to the point in which the two systems exhibit diverging mechanisms, i.e., the specimens reach even higher toughness modulus values and extensibilities than those indicated here. The toughness modulus is defined as the area under the stress strain curve and is a widely used metric for the fracture resistance of biological materials.[11] With exception of the bio-calcite-like geometry (for reasons stated above), the trends of the mechanical properties have a very good agreement between experiment and simulation. The simulation prediction agrees with the experimental observation that the rotated bone-like topology is the most compliant and the most extensible. Furthermore, our predictions about the relative strength of the bone-like geometry and rotated bone-like geometry are also compatible with experiment. Finally, our computational model is able to correctly identify the toughest topological arrangement as the bone-like geometry, and the experiment shows that this system achieves a toughness modulus more than 20 times that of its constituents, a truly impressive result.

several ways we could refine our approach to ensure a better agreement between topologies in experiment and simulation. The most apparent strategy is to increase the feature size at printing. Another, and possibly more appealing, solution is to print the samples vertically, with their thinnest dimension parallel with the 'build tray' as the machines perform with higher precision in this dimension.

We note that both the prediction of our computational model and the experimental result for the response of the bio-calcite-like system presented here differs from that presented in our previous study, where the composite system had a lower stiffness ratio and we predicted brittle fracture of the system. This is consistent with a recent study where we found that composites exhibit sudden transitions in deformation and fracture mechanisms as the constitutive relations of their constituents are tuned.[34] The stiffness ratio between the

2.2. Experimentally Observed Fracture Mechanisms

We present snapshots of the entire fracture process of the bone-like specimen in **Figure 7**. Figure 7c shows the crack propagating in a step pattern around the stiff platelets and through the continuous compliant matrix. The application of energy principles predict that a crack will choose the path of least resistance, i.e., the most energetically favorable path. Furthermore, by applying linear elastic fracture mechanics to the sample at hand we realize that in order to satisfy the above principle, the crack path will result as a trade-off between the minimum crack deflection angle and the path of least stiffness. Figure 7c shows that the crack propagates perpendicularly to its original orientation, choosing a longer path and propagating exclusively through the compliant matrix with stable crack propagation as a result. By the

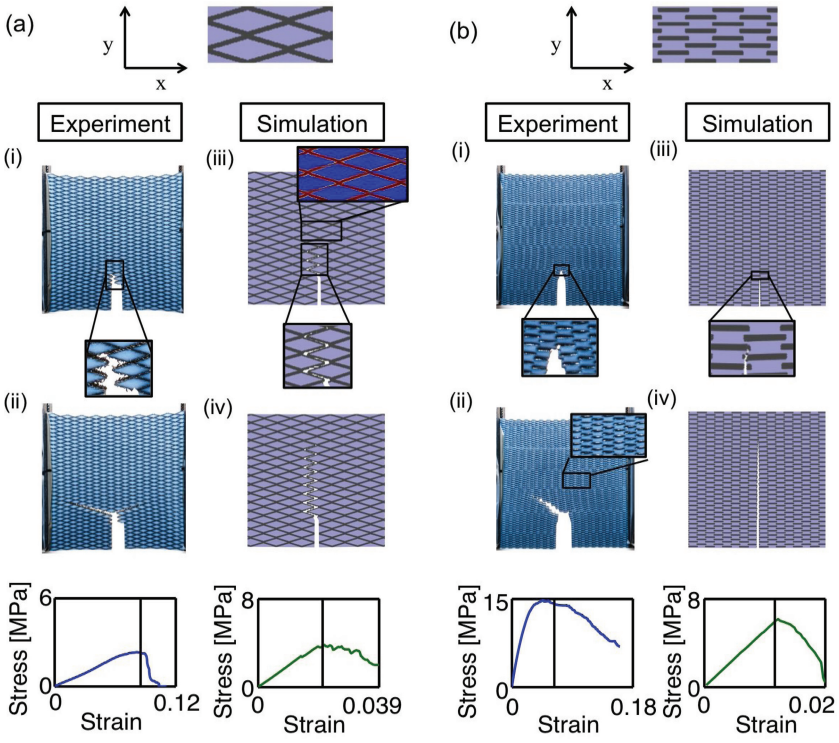

Figure 5. Visualization of dominating deformation and fracture mechanisms in experiment and simulation for a) the rotated bone-like geometry and b) the bio-calcite-like geometry in addition to the respective stress-strain responses, again with blue and green indicating results from experiment and simulation respectively. Schematics of the topologies are included at the top. a) displays the characteristic zigzag fracture path observed both in the simulation and for the initial propagation in experiment. As the effective length of the sample decreases the eccentricity of the applied load increases, changing the boundary conditions and thus causing predictions from experiment and simulation to diverge. As is apparent from the displayed images, for both simulation and experiment, the compliant phase forces the crack to take a longer path thus inducing toughening in the rotated bone-like specimen. The stress strain responses also reveal that we correctly predict a very compliant behavior of this topology. b) indicates that the simulation predictions and experimental observations for the bio-calcite-like topology do not overlap very well. The inset in (b) (ii) shows inaccuracies in the printing that are likely a contributing factor. Nonetheless, we do observe a similar toughening mechanism in experiment and simulation in that both systems show an initial crack arrest and crack blunting in a soft inclusion; (i), (iii). The printed specimens are all 3.125 mm thick in the out of plane direction.

considerations above, this toughness mechanism is clearly activated by the combination of the major stiffness mismatch between material **A** and material **B** and their specific topological arrangement. Furthermore, in Figure 7d we likely see the influence of the boundary on fracture propagation as its presence seemingly inhibits the initial mechanism to continue and the crack suddenly propagates through a set of rows of stiff platelets. At this point, the sample has incurred substantial damage, and we observe platelets breaking away from the crack tip. We thus receive further confirmation that the stress field is strongly delocalized, resulting in an efficient usage of the material throughout the sample. Furthermore, Figure 7e,f indicate repetitions of the initial fracture mechanism observed in Figure 7c,d. The composite exhibits impressive toughness (Figure 6a). The failure process exhibited by the bone-like sample, detailed here and portrayed in Figure 7, is reminiscent of the mechanical failure of natural mineralized composites.[2,5,10,13,35]

Figure 8 displays the fracture process in the rotated bone-like specimen. In Figure 8b we clearly see the influence of the compliant phase in postponing the main fracture propagation by blunting the crack tip. As the stress concentration scales with the inverse square root of crack tip radius, the compliant phase acts to reduce the intensity of the stress field at the notch. Upon reaching a critical deformation the fracture propagates and does so in a characteristic zigzag pattern. Again, as for the bone-like specimen, it is energetically more favorable for the crack to propagate through the compliant matrix and thus is forced through the longer route around the stiff rhombus shaped inclusions, contributing to additional energy dissipation. As the crack propagates, the eccentricity of the applied load increases, resulting in additional moment loading on the sample. This leads to crack branching, where the fracture propagates from the crack tip along diagonals through the compliant matrix (Figure 8d). Eventually, one of the crack branches starts to dominate and propagates through to the boundary quickly resulting in complete failure of the composite (Figure 8e,f).

Finally, we show snapshots of the complete fracture process in the bio-calcite-like specimen (**Figure 9**). Unlike the bone-like specimen and the rotated bone-like specimen, the stiff phase is the matrix in the bio-calcite-like topology. This has a marked effect on crack propagation. There is no continuous soft phase for fracture to propagate through, and it is thus forced to move through the stiffer matrix. The crack attempts to minimize the distance it travels through the stiffer phase thus resulting in a rugged fracture surface. The fracture propagates in a staccato like manner with consecutive crack arrest and crack propagation. Eventually the crack propagates into the boundary and the specimen is unloaded. As is displayed in Figure 6a, these mechanisms lead to the impressive fracture mechanical characteristics of the specimen.

3. Conclusion

With the use of 3D printers we made the leap from computationally designed bio-inspired composite materials with predicted fracture response far exceeding that of their fundamental constituents to synthetic composites with similar mechanical characteristics. Our predictions from simulation

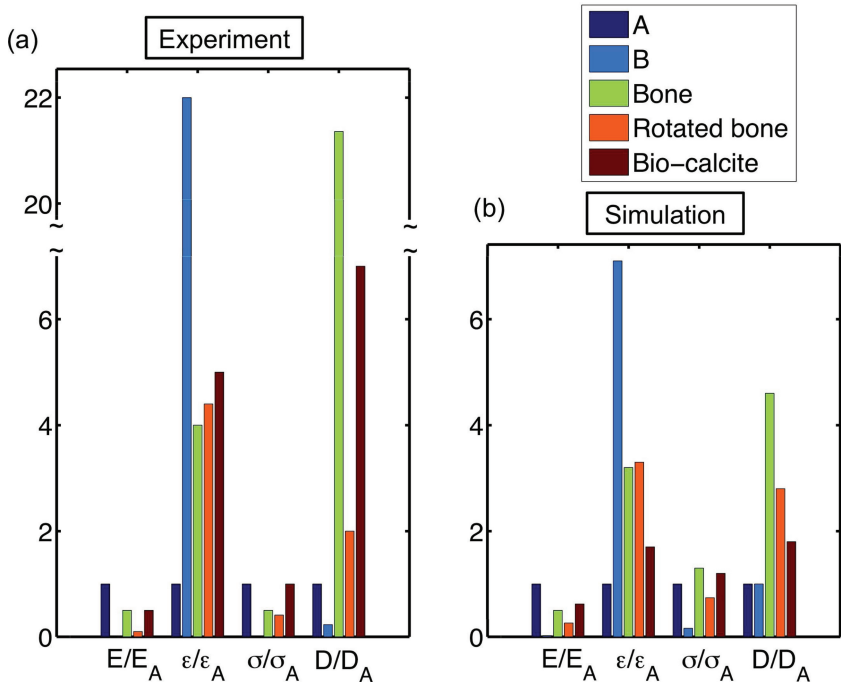

Figure 6. Bar plot indicating trends of mechanical properties for the base materials and the various topologies studied in both a) experiment and b) simulation. We perform the comparison using data from experiment and simulation up to the point in which the two systems exhibit diverging mechanisms; these instants are displayed in Figure 4 and 5. For the simulation data, A and B refer to the computational equivalents of material **A** and material **B** as presented in Figure 3. We plot stiffness E, maximum strain ε, maximum stress σ, and toughness modulus D. In (a) the data is, as indicated, normalized by the respective values for the base material **A** while in (b) the data is normalized by the respective values for the computational equivalent of the base material **A**. The Figure portrays that, with the exception of the bio-calcite-like sample for reasons stated above, the mechanical properties of the simulated materials exhibit the same trends as those of the synthesized materials, *i.e.,* our models predict the correct composite to be the most extensible, strongest and toughest. Furthermore, we observe the largely impressive fracture toughness of the synthesized bone-like specimen exceeding that of its fundamental building blocks by a factor larger than 20.

agreed well with the trends we observed in experiment, and the synthesized composites exhibited fracture mechanical properties such as toughness modulus an order of magnitude larger than its fundamental building blocks. By printing composites from base materials (that have widely contrasting constitutive behavior and which each exhibit brittle fracture behavior) in specific topological arrangements, we created structures that feature significant toughening mechanisms and stable crack propagation.

Our contribution is a first attempt at utilizing 3D printers to create mechanically tough bio-inspired composites from simple building blocks and at using computational models to predict the response of 3D printed structures. This research can potentially pave the way for more refined computational models able to predict the response of 3D printed systems with higher accuracy as well more complex 3D printed structures with further improved mechanical properties. We have already identified several potential refinements and improvements on both modeling and printing that could propel this effort forward. Moreover, as 3D printers evolve, we as designers will seize more control over the manufacturing process allowing composites to be synthesized at even finer length scales, with more details and increased control of constituent material properties, opening the doors for the rapid manufacturing of structurally advanced complex multi-hierarchy biomimetic materials with applications in a large range of engineering disciplines. In future works we might consider printing larger specimens with more repeat units of the topological unit cells to avoid the boundary interfering with the fracture path. Further studies to understand the connection between experimental and computational results are needed, including an analysis of the effects of different stiffness ratios between the two phases. A systematic gradation of the level of contrast between the two components could be carried out and shed further light into the mechanics of bioinspired composites.

4. Experimental Section

Synthesis: All specimens used in the study were printed at Stratasys Ltd., in Billerica, MA, USA using an Objet Connex500 multi-material 3D printer. In a single print we manufactured composites composed of two base materials, VeroWhitePlus and TangoBlackPlus, with strongly contrasting material properties (Figure 3). Both VeroWhitePlus and TangoBlackPlus are photopolymers, based upon proprietary acrylic-based photopolymer resins, and we will henceforth refer to them as material **A** and material **B**, respectively. We printed the geometries developed and modeled in a previous study and for completeness include schematics of the topological arrangements in Figure 2a. The lighter phase represents the stiffer constituent and was printed with material **A**, and the darker phase, representing the compliant constituent, was printed with material **B**. Figure 2b indicates the planar dimensions of the test specimen. The through thickness of all geometries is 3.125 mm and the thickness of the soft phase in all composites is 250 μm.

The composites were printed with a dual material jetting technology allowing two distinct materials to be printed simultaneously. Each material, residing in cartridges, is funneled through a liquid system connected to the printing block consisting of eight printing heads. Two printing heads, each containing 96 nozzles with 50 μm diameters, are reserved for each of the two base materials, while the remaining four printing heads are used for printing a support material. The printing heads are followed by a UV light that immediately cures the printed material allowing new layers to be printed instantaneously. We printed three specimens of each composite system detailed in Figure 2 and used one of each geometrical configuration as test specimens to arrive at a suitable experimental approach. The remaining six samples were used for mechanical testing and investigation of deformation and fracture mechanisms.

As the materials cure in situ upon printing, they adhere to each other perfectly, i.e., the adhesion is as strong as or stronger than the

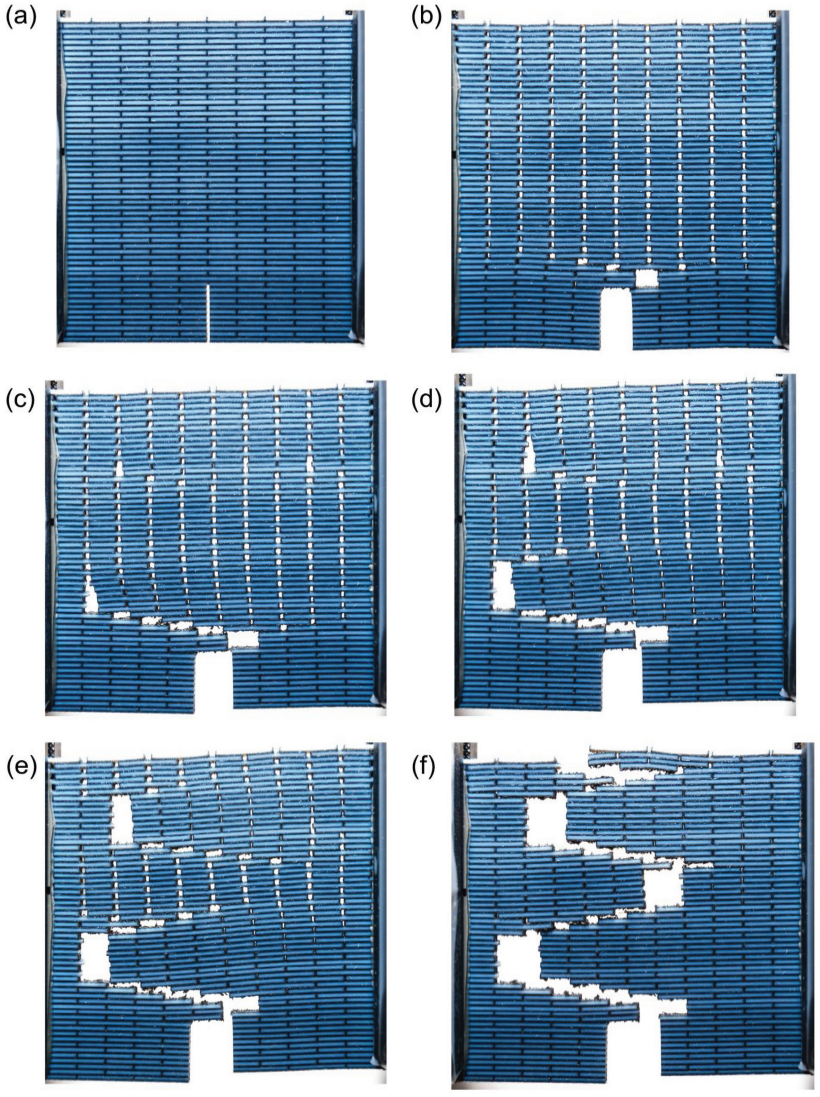

Figure 7. a–f) Snapshots of fracture propagation in the synthesized bone-like specimen. Images clearly show two dominating toughening mechanisms exhibited by the printed composite. The second snapshot indicates a delocalized load transfer in the topology with damage being sustained away from the crack tip. Furthermore, we observe a pronounced crack deflection mechanism induced by the particular topological arrangement of the two base materials with widely contrasting constitutive behavior. This causes the crack to take a long path through the specimen thus dissipating large amounts of energy on the way. Moreover, as the fracture mainly propagates through the extremely compliant base material **B** the crack is blunted, leading to a lesser stress concentration at the crack tip and thus stable fracture propagation.

weakest phase, and we confirmed this by observing that failure never initiates nor ever occurs at the interface of the base materials. The smallest feature size of the compliant phase in our prints is 250 μm and is identical for all samples; the compliant phase is indicated in black in Figure 2a and the smallest feature of the compliant phase for all geometries is its in plane thickness. The nozzle diameter controls the accessible length scale of the 3D printing. Since we predicted that the specific topological arrangements of the base materials strongly influence the composites mechanical response, it is essential to ensure precise printing, thus justifying the feature size being a multiple of the nozzle diameter. This implies a larger length scale than that associated with our previous computational investigations, and we comment on this below.[32] At this length scale all topologies except the bio-calcite-like topologies were recreated well. In addition to the interfacial mixing effect mentioned earlier, we suspect the inaccuracies may have to do with limited resolution of the printers. The soft inclusions in the bio-calcite-like topology are significantly smaller than the stiff inclusions in the bone-like topology.

Fracture Testing: The specimens were tested as single edged notched tensile specimens. The notches in the samples were cut so that all samples have an identical effective size in the dimension parallel to the crack direction, i.e., the uncracked length in the *z*-direction is the same for all samples (Figure 2). The notches were cut with a 1/32" (0.79 mm) thick carbide-slitting saw with a 60° included angle. When testing the sample specimens, initial crack propagation always occurred at the crack tip, thus indicating that the machined notches are sufficiently sharp.

For optimal gripping of the specimens in the testing apparatus we attached four aluminum strips to each sample with Loctite E-90FL epoxy, two on either face of the planar specimen. We roughed the aluminum with sand paper to ensure optimal adhesion of the Loctite epoxy and allowed the epoxy to cure for 36 h. The aluminum strips were positioned such that all samples had the same effective length (Figure 2).

We tested the 3D printed specimens in an Instron 5582 Universal Testing Machine with an Instron 100 kN static load cell and applied displacement boundary conditions. The samples were clamped in place with serrated hardened steel grip faces attached to steel vice action grips. The load capacity of the grips is 100 kN and the spring stiffness of the entire testing device far exceeds the stiffness of our specimens. We attached our specimens firmly in the grips and center the uncracked length of the geometries with the force applied through the vice action grips to ensure pure tension in the specimens prior to initial crack propagation. We did this to emulate the displacement boundary conditions applied in our computational investigations as closely as possible. However, it is clear that upon initial crack propagation, the specimen will no longer be subjected to pure tension, as the force will be acting with an eccentricity on the remaining uncracked length of the test specimen. The moment induced by the eccentricity influences the near tip stress field of the geometries and thus leads to a different loading than a pure tension boundary condition would.

In the experimental setup we employed a displacement rate of 3 mm/min. The compliant base material is very extensible and a much slower loading rate would require an exorbitant amount of time for testing. Typically, a high strain rate leads to brittle response of testing specimens, but the observation of stable crack propagation in our samples assures us that we still capture essential deformation and fracture mechanisms with our testing procedure.

We emphasize that the testing procedure adopted in this study is not meant to emulate a standard procedure as outlined in ASTM; rather we looked to employ an approach that is both similar to our computational investigations and suited for investigating fracture and deformation mechanisms. Our main focus was to keep

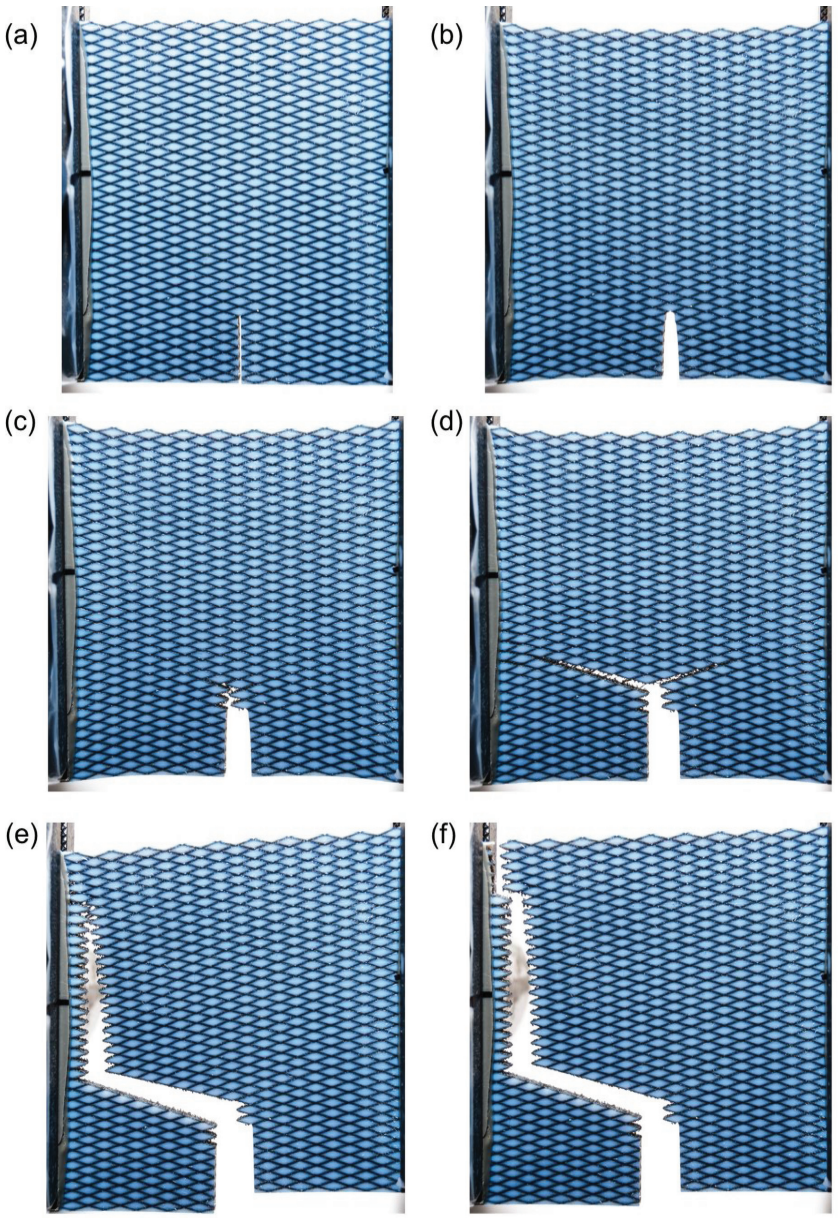

Figure 8. a–f) Snapshots of fracture propagation in the synthesized rotated bone-like specimen. The second snapshot indicates the significant deformability of the composite in the presence of the crack; an apparent blunting of the crack-tip highlights this. We further observe the characteristic zigzag pattern of fracture propagation in (c) made possible by the extreme compliance of the matrix phase combined with the specific composite topology. As the eccentricity of the applied load increases we observe a crack branching in panel (d), followed by a dominating crack propagating to and along the boundary in (e) resulting in complete failure of the composite.

our testing procedure consistent and similar to a setup we could emulate with our computational model, as the insights gained from this study derive from a comparative study of the deformation mechanisms of the manufactured specimens and simulated specimens.

Material Properties of Base Materials: Selections of bulk mechanical properties of the Objet printable materials have already been made available. The referenced data indicates that of the materials available for printing, the two employed in this study represent the most contrasting mechanical behavior. Although this causes some difficulties for our computational modeling, material **A** and material **B** were still utilized as this made for a more straightforward printing. In future work it would be very interesting to explore more material combinations. No previous data exists on the stiffness of material **B** and thus we performed mechanical tests on both base materials in order to supply data to our computational model. As we were also interested in the fracture response of these materials, we performed fracture tests with the same procedure as detailed above. Images of the samples pre- and post-testing along with their stress-strain responses are presented in Figure 3. The Figure clearly shows the widely contrasting constitutive behavior of the two materials. Indeed, the modulus of the compliant material **B** is three orders of magnitude lower than the stiffer material **A**, by a factor of ≈1500. Furthermore, the more compliant base material failed at an order of magnitude higher strain than its less compliant counterpart, and both samples failed in a brittle manner immediately upon crack propagation.

Computational Modeling: We conducted computational investigations of the experimentally manufactured and tested specimens. To this end we used a previously developed meso-scale model with proven capability of capturing fundamental deformation and fracture mechanisms found in bio-mineralized materials.[17,32,33] As mentioned above, the topologies in this study exist at a larger length scale than for those the model was developed. However, with the appropriate rescaling of constitutive relations, our model can be trained to access the larger length scale relevant here. Indeed we argue that it is still sensible to model the system as a discrete network for the purpose of investigating its fracture mechanics.[36] In the following we present the material model utilized and the rationale behind it.

As the base materials cure during printing there is likely a certain amount of mixing present at the interface. With the small relative size of the compliant phase and the large difference in modulus of the two materials, the effective stiffness ratio is clearly far less than what is portrayed in Figure 3. In a simplified model we can view the effective compliant phase as a layered composite of material **A** and material **B** and can use Voigt's rule of mixtures to find its true stiffness. Assuming an approximate 3–4% mixing of the two base materials at the interface we estimated an effective stiffness ratio between 45 and 60, as opposed to ≈1500, and we used a stiffness ratio of 50 for our computational model. The true stiffness of the compliant phase could also have been measured directly with the use of a micro- or nanoindenter. Using a test-apparatus with sufficient resolution would also give insight to the amount of interfacial mixing of the base materials. However, in an effort to keep our model simple, we found it more appropriate to represent the system with the Voigt's rule derived effective stiffness ratio discussed above. In future work we can consider extending our model to account for the true stiffness distribution in the compliant phase as measured by indentation.

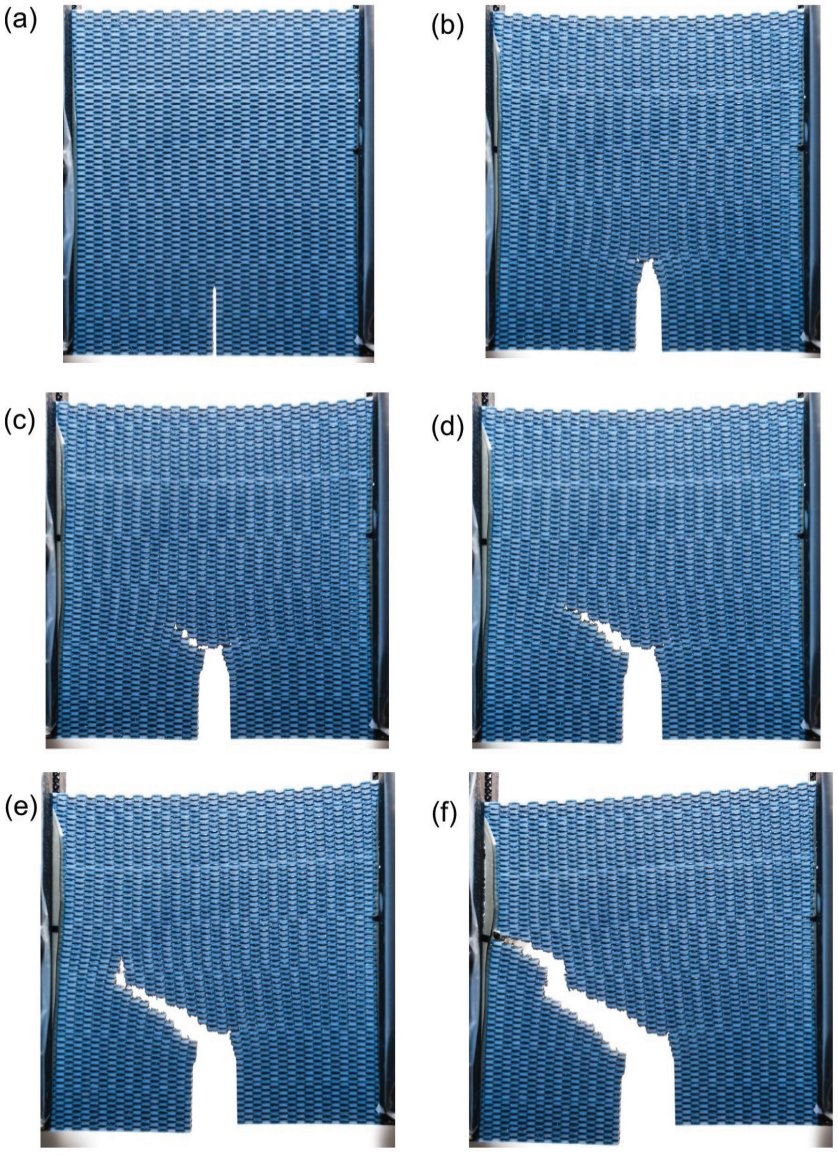

Figure 9. a–f) Snapshots of fracture propagation in the bio-calcite like specimen. As for the rotated bone-like specimen we observe the specimen undergoing significant deformation prior to major crack propagation, enabled by the crack-tip blunting displayed in (b), this was also highlighted in Figure 5. In (c) the crack has started to propagate towards the boundary and eventually reaches it in (f). The crack propagates slowly through the sample undergoing significant deformation in the process. We clearly observe that the compliant phase influences the crack propagation path and leads to toughening in the composite indicated by the resulting rough fracture surface.

Independent mechanical tests report extensibilities of material **A** and material **B** ranging from 10–25% and 170–220%, respectively. From a purely geometrical perspective it is quite clear that the utilized triangular lattice becomes highly non-linear and unstable at such large deformations, and it is advantageous to restrict the allowable deformation. It is also clear that the deformability of the compliant phase is an essential feature of the composite and indeed plays an active role in the mechanics of natural mineralized materials. Our experience with harmonic spring bead triangular lattice models indicates that 5% is a suitable minimal breaking strain. In order to maximize the extensibility of the compliant phase without compromising the stability of the model, we thus adopted this failure strain for the computational equivalent of material A. We further chose the deformability of the compliant phase such that the toughness modulus of the composite constituents is identical. The resulting extensibility of the computational representation of material B is thus 35%, and the notched stress strain responses of the two model materials are given in Figure 3b.

The base materials used in this study are photopolymers, and although they behave linearly under the presence of a pre-crack (Figure 3b), their bulk constitutive relations are highly nonlinear. As this study represents a first effort to predict the behavior of the 3D printed system, we restricted our computational material models to linear elasticity (Figure 3b). Our main focus in this paper is to predict and understand trends in the deformation and fracture response of the printed composites and we therefore found it sensible to start with such a simplified model. Although the specific nonlinearities of the photopolymers will clearly influence the particular crack propagation, we argue that the dominating fracture and deformation mechanisms will mainly depend on the stiffness ratio and relative extensibilities of the composite constituents, thus validating our model selection. In future works our model can be extended to account for the nonlinearities of the printed materials and thus could be used for quantitative predictions of the printed systems response.

Acknowledgements

We acknowledge funding from the Army Research Office (W911NF-10-1-0127). We thank Pierce Hayward and Stephen Rudolph (both MIT) for help with the experimental testing. L.D. and M.J.B. designed the research, conceived and implemented the concept, analyzed the data and developed the conclusions. i.e., and L.D. 3D printed the specimens. L.D. and G.B. carried out the mechanical testing, imaging, and collected the data. L.D. and M.J.B. wrote the paper with input from all co-authors.

Received: January 19, 2013
Revised: May 4, 2013
Published online: June 17, 2013

[1] J. Aizenberg, J. C. Weaver, M. S. Thanawala, V. C. Sundar, D. E. Morse, P. Fratzl, *Science* **2005**, *309*, 275.
[2] F. Barthelat, *Bioinspiration Biomimetics* **2010**, *5*, 035001.
[3] M. J. Buehler, *Nanotechnology* **2007**, *18*, 295102.
[4] J. D. Currey, *Science* **2005**, *309*, 253.
[5] P. Fratzl, H. S. Gupta, E. P. Paschalis, P. Roschger, *J. Mater. Chem.* **2004**, *14*, 2115.
[6] P. Fratzl, R. Weinkamer, *Prog. Mater. Sci.* **2007**, *52*, 1263.
[7] H. S. Gupta, J. Seto, W. Wagermaier, P. Zaslansky, P. Boesecke, P. Fratzl, *Proc. Natl. Acad. Sci. USA* **2006**, *103*, 17741.

[8] C. E. Hamm, R. Merkel, O. Springer, P. Jurkojc, C. Maier, K. Prechtel, V. Smetacek, *Nature* **2003**, *421*, 841.
[9] M. Hildebrand, *Chem. Rev.* **2008**, *108*, 4855.
[10] S. Kamat, X. Su, R. Ballarini, A. H. Heuer, *Nature* **2000**, *405*, 1036.
[11] G. Mayer, *Science* **2005**, *310*, 1144.
[12] M. A. Meyers, P. Y. Chen, A. Y. M. Lin, Y. Seki, *Prog. Mater. Sci.* **2008**, *53*, 1.
[13] P. Fratzl, H. S. Gupta, F. D. Fischer, O. Kolednik, *Adv. Mater.* **2007**, *19*, 5597.
[14] H. J. Gao, B. H. Ji, I. L. Jager, E. Arzt, P. Fratzl, *Proc. Natl. Acad. Sci. USA* **2003**, *100*, 5597.
[15] B. H. Ji, H. J. Gao, *J. Mech. Phys. Solids* **2004**, *52*, 1963.
[16] K. Okumura, P. G. de Gennes, *Eur. Phys. J. E: Soft Matter Biol. Phys.* **2001**, *4*, 121.
[17] D. Sen, M. J. Buehler, *Sci. Rep.* **2011**, *1*, 35.
[18] S. M. Douglas, H. Dietz, T. Liedl, B. Hogberg, F. Graf, W. M. Shih, *Nature* **2009**, *459*, 414.
[19] E. Dujardin, S. Mann, *Adv. Mater.* **2002**, *14*, 775.
[20] T. L. Sun, L. Feng, X. F. Gao, L. Jiang, *Acc. Chem. Res.* **2005**, *38*, 422.
[21] Z. Y. Tang, N. A. Kotov, S. Magonov, B. Ozturk, *Nat. Mater.* **2003**, *2*, 413.
[22] Y. Wang, A. S. Angelatos, F. Caruso, *Chem. Mater.* **2008**, *20*, 848.
[23] F. Xia, L. Jiang, *Adv. Mater.* **2008**, *20*, 2842.
[24] D. Bak, *Assembly Autom.* **2003**, *23*, 340.
[25] D. Dimitrov, K. Schreve, N. de Beer, *Rapid Prototyping J.* **2006**, *12*, 136.
[26] H. Seitz, W. Rieder, S. Irsen, B. Leukers, C. Tille, *J. Biomed. Mater. Res. B* **2005**, *74B*, 782.
[27] E. A. Roth, T. Xu, M. Das, C. Gregory, J. J. Hickman, T. Boland, *Biomaterials* **2004**, *25*, 3707.
[28] C. X. F. Lam, X. M. Mo, S. H. Teoh, D. W. Hutmacher, *Mater. Sci. Eng., C* **2002**, *20*, 49.
[29] K. F. Leong, C. M. Cheah, C. K. Chua, *Biomaterials* **2003**, *24*, 2363.
[30] B. W. Miller, J. W. Moore, H. H. Barrett, T. Frye, S. Adler, J. Sery, L. R. Furenlid, *Nucl. Instrum. Methods* **2011**, *659*, 3397.
[31] A. Park, B. Wu, L. G. Griffith, *J. Biomater. Sci.* **1998**, *9*, 89.
[32] L. S. Dimas, M. J. Buehler, *Bioinspiration Biomimetics* **2012**, *7*, 036024.
[33] D. Sen, M. J. Buehler, *Int. J. Appl. Mech.* **2010**, *2*, 699.
[34] L. S. Dimas, M. J. Buehler, *J. Mater Res.*, **2013**, *28*, 1295.
[35] J. Y. Rho, L. Kuhn-Spearing, P. Zioupos, *Med. Eng. Phys.* **1998**, *20*, 92.
[36] W. A. Curtin, H. Scher, *J Mater Res* **1990**, *5*, 554.